A Thermally Robust Porous Basalt Foam for Elevated-Temperature Acoustic Absorption

Muhammad Imran, Hongjun Fan, Tenglong Xu, Xiaobing Cai*

State Key Laboratory for Strength and Vibration of Mechanical Structures, School of Aerospace Engineering, Xi'an Jiaotong University, Xi'an 710049, China.

Abstract: High-temperature sound absorbers are required for thermally severe environments where acoustic attenuation must remain effective during heat exposure. Here, a porous Basalt Foam (BF) was fabricated through Tween 80-assisted fiber dispersion, sodium silicate-mediated local bonding, layer-by-layer assembly, and controlled compaction. The resulting foam combined low bulk density, high porosity, localized binder bonding, and an interconnected fibrous pore network. Direct flame exposure showed localized heating followed by rapid cooling, while the foam retained its structural integrity. SEM analysis confirmed that sodium silicate mainly formed local joints at fiber-fiber contact points without blocking the open porous framework. Acoustic testing using an impedance tube showed that sound absorption was strongly dependent on frequency, thickness, and temperature. The 25 mm BF maintained effective absorption at 100, 300, and 500 °C, while the 50 mm BF showed strong absorption at 200, 400, and 600 °C. Thicker samples provided broader and more stable absorption due to longer acoustic pathways and enhanced viscous/thermal dissipation within the tortuous fiber network. Compression testing further confirmed structural integrity, with partial recovery after large deformation. Overall, the developed BF offers a simple, lightweight, inorganic, and thermally robust porous architecture for high-temperature noise-control applications.

Keywords: Basalt fiber foam; Elevated-temperature acoustics; Porous sound absorber; thermal resistance; Flame-resistant materials; Multifunctional insulation.

INTRODUCTION

The development of sound-absorbing materials that can maintain reliable performance at elevated temperature has become an important challenge in modern engineering systems(Li *et al.* 2021). This need is especially clear in aerospace propulsion, where acoustic liners are used as a major passive strategy for suppressing aero-engine noise, yet the liner material must work under combined thermal, flow, and mechanical loading(Spillere *et al.* 2021; Qi Zhang *et al.* 2025). Similar requirements also arise in hot exhaust ducts, combustion-related systems, and other industrial environments where noise reduction cannot be separated from thermal resistance. Earlier work on aircraft-engine materials and later reviews on aero-engine liner technology both show that high-temperature acoustic behavior is not a secondary consideration, but a practical design requirement for real service conditions(Ma & Su 2020; Paun, Gasser, & Leylekian 2003).

From an acoustic standpoint, porous and fibrous absorbers remain particularly attractive because incident sound waves can enter their interconnected pore channels and gradually lose energy through viscous friction, thermal exchange, and repeated internal scattering(Chen *et al.* 2020; Li *et al.* 2026; Lomte *et al.* 2024). In comparison with many resonance-based absorbers, which are usually effective over relatively narrow frequency bands, porous media are better suited to broadband dissipation because the energy-loss process is distributed throughout the internal structure(Cheng *et al.* 2022). Reviews on porous and fibrous sound absorbers further show that their performance depends strongly on structural parameters such as thickness, porosity, pore size, tortuosity, permeability, and airflow resistivity. In practice, these materials are usually most effective in the medium- and high-frequency range unless the internal architecture is carefully tuned to improve low-frequency absorption(Cao *et al.* 2018; Feng & Liu 2025; Tang & Yan 2017).This means that the design of a high-temperature absorber cannot rely on chemistry alone; the pore architecture must also be controlled with equal care.

Because of these requirements, a large part of recent research has moved toward inorganic and ceramic sound-absorbing systems. Hierarchically structured ceramic nanofibrous aerogels have been reported to combine fire resistance, elasticity, and efficient low-frequency noise reduction, while bubble-templated ceramic nanofiber aerogels have shown that high-temperature noise absorption can be achieved in lightweight all-ceramic architectures(Bai *et al.* 2019; Cao *et al.* 2022; Zong *et al.* 2022). Related progress has also been made in multifunctional SiC/SiO_2 nanofibrous

*Address correspondence to this author at the State Key Laboratory for Strength and Vibration of Mechanical Structures, School of Aerospace Engineering, Xi'an Jiaotong University, Xi'an 710049, China; E-mail: caixiaobing@xjtu.edu.cn

aerogels and in fibrous porous mullite ceramics, where thermal insulation, flame resistance, and sound absorption are addressed together rather than independently(Peng Zhang *et al.* 2025). In addition, porous ceramics with tailored pore architectures and layered ceramic fibrous membranes have further demonstrated that microstructural design can improve acoustic response while preserving thermal robustness(Lou *et al.* 2023; Yang *et al.* 2024). These studies make it clear that current high-temperature acoustic materials are moving toward porous inorganic systems in which fiber networks, pore pathways, and local reinforcement features are jointly engineered.

Among inorganic fibrous materials, basalt fiber is particularly relevant because it combines mineral origin, thermal stability, nonflammability, and good chemical durability with a comparatively simple materials base(Fiore *et al.* 2015; Jamshaid & Mishra 2016). Basalt-based porous panels have already shown useful thermal and acoustic performance in building-related applications(Buratti *et al.* 2015; Moretti, Belloni, & Agosti 2016). More recently, basalt-containing lightweight absorbers such as cellulose/basalt composite paper have demonstrated broadband sound absorption together with low thermal conductivity, highlighting the ability of basalt fibers to regulate pore structure and heat-transfer pathways(Song *et al.* 2024). At the same time, review work on fibrous absorbers notes that inorganic fibers including basalt have already drawn attention for noise-reduction applications because of their porous structure and durability(Tang & Yan 2017). Even so, much of the accessible basalt-fiber literature still remains focused on building insulation, composite panels, or room-temperature acoustic evaluation. That leaves a practical gap for a simpler porous basalt-fiber absorber that can be fabricated by a straightforward route and then examined directly under elevated-temperature acoustic conditions. This gap is particularly meaningful for thermally severe engineering fields, including aerospace, where both heat tolerance and acoustic performance are required in the same material.

In this work, a porous Basalt Foam (BF) was fabricated from chopped basalt fibers through Tween 80-assisted dispersion, sodium-silicate-mediated local bonding, layer-by-layer assembly, and controlled compaction. Rather than relying on more elaborate ceramic aerogel routes, the present approach was intended to establish a comparatively simple way to construct a thermally stable porous fibrous architecture. The fabricated foam was then evaluated from three complementary perspectives. First, its thermal response under direct flame exposure was examined to assess localized heating, cooling behavior, and structural integrity. Second, its microstructure was characterized to clarify the porous fiber network, local binder distribution, and fiber-scale features of the resulting foam. Third, its normal-incidence sound absorption behavior was investigated at room temperature for different sample thicknesses and at elevated temperature for a 50 mm sample. Through this combined investigation, the study aims to determine whether a relatively simple basalt-fiber porous material can provide a useful balance of open porosity, thermal resistance, and acoustic attenuation for high-temperature sound-control applications. The broader significance of this approach lies in its potential relevance to thermally demanding aerospace and industrial environments, where lightweight porous materials are expected to tolerate heat while continuing to dissipate sound.

The remainder of this paper is organized as follows. Section 2 describes the raw materials, fiber dispersion treatment, foam fabrication procedure, thermal testing, microstructural characterization, and sound absorption measurements. Section 3 presents and discusses the thermal response, SEM observations, room-temperature sound absorption behavior at different thicknesses, and the elevated-temperature acoustic performance of the BF. Finally, Section 4 summarizes the main findings and the engineering significance of the developed material.

MATERIALS AND METHODS

The BF samples were fabricated through a sequential process that included surface treatment and separation of the chopped basalt fibers, manual placement of the fibers in a circular mold, application of a sodium silicate-based binder, and subsequent compression using a piston-cylinder arrangement to build the structure layer by layer. After compaction, the fiber preform was thermally treated to remove moisture and consolidate the binder, thereby promoting bonding between adjacent fibers and forming a porous BF. Following fabrication, the thermal response of the prepared foam was first evaluated under direct flame exposure and compressive behavior was also evaluated. The morphology of the treated basalt fibers and the inter-fiber bonding within the foam structure were then examined by scanning electron microscopy (SEM). Finally, the acoustic performance of the prepared samples was evaluated using an impedance tube under both ambient and elevated temperature conditions, including the room-temperature behavior of samples

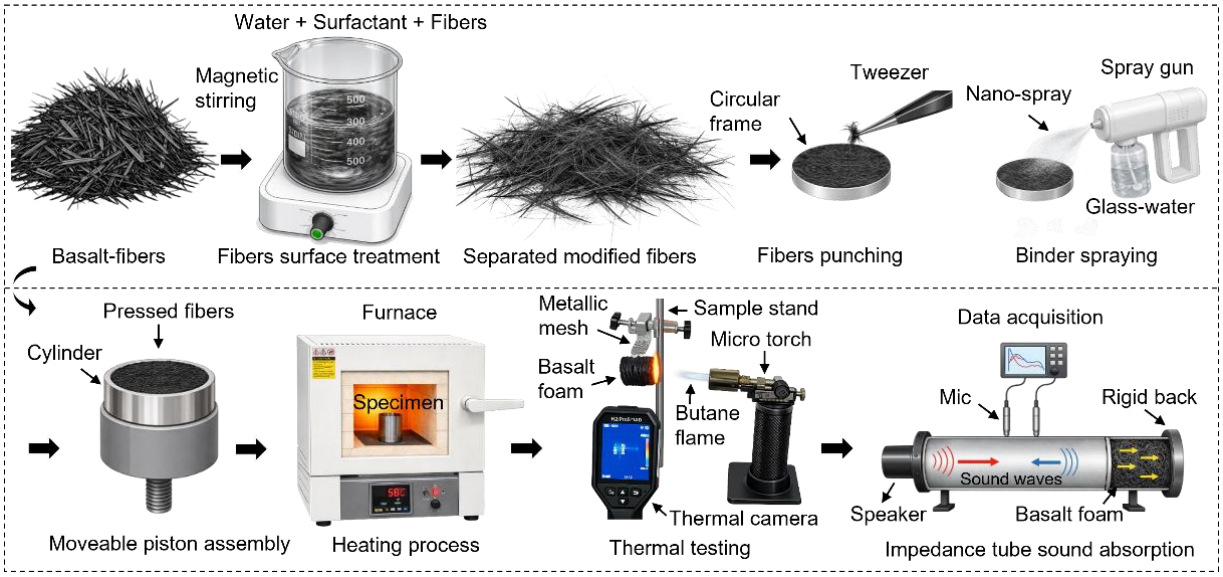

Figure 1: Schematic illustration of the fabrication process of basalt foam from surface-modified chopped basalt fibers and its subsequent acoustic characterization using an impedance tube.

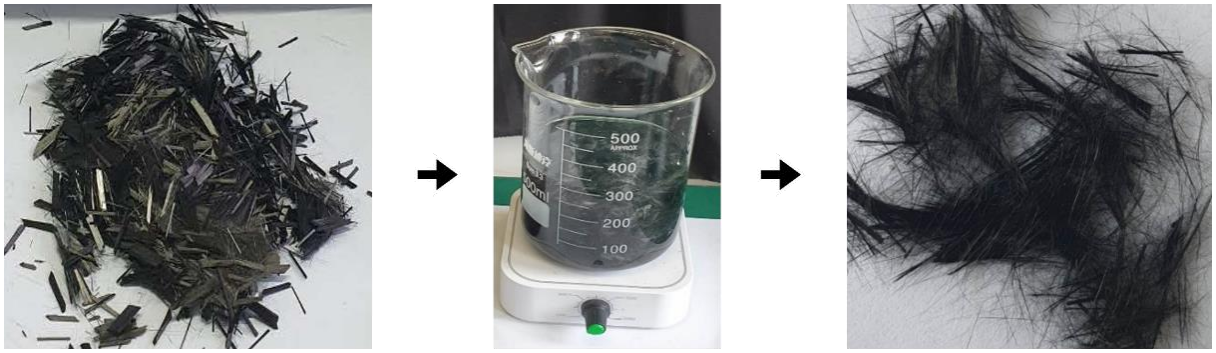

Figure 2: Tween 80-assisted dispersion process of basalt fibers: untreated chopped fibers, treatment in aqueous Tween 80 solution, and separated fibers after modification.

with different thicknesses, the high-temperature sound absorption of the 50 and 25 mm samples, and the comparison between room- and high-temperature acoustic responses. The overall experimental procedure, including fabrication, thermal testing, and acoustic evaluation, is schematically illustrated in Fig. **1**.

Tween 80-Assisted Dispersion of Basalt Fibers

Tween 80 was used as a nonionic surfactant to improve the dispersion of basalt fibers and reduce fiber agglomeration during processing(Kang & Jeong 2015). For the surface treatment, 5 g of chopped basalt fibers were dispersed in 300 mL of water containing 3 mL of Tween 80. The suspension was then stirred using a magnetic stirrer at 2000 revolutions per minute (rpm) for 5 min, with a magnetic stirring bar of approximately 2.5 cm × 0.8 cm. The selected Tween 80 concentration and stirring conditions were consistent with a previous fiber-dispersion study in which Tween 80 was used as a nonionic surfactant for aqueous glass-fiber dispersion, with a surfactant content of 2 wt.% and mixing at 2000 rpm(Wang *et al.* 2023). In the present study, 3 mL Tween 80 in 300 mL water and stirring at 2000 rpm for 5 min were selected to achieve sufficient wetting and separation of basalt fiber bundles while avoiding excessive foaming, fiber entanglement, or breakage. Therefore, these conditions provided a practical and reproducible processing window for preparing uniformly dispersed basalt fibers before foam fabrication. During this process, Tween 80 molecules were physically

adsorbed onto hydroxylated sites on the basalt fiber surface through weak intermolecular interactions, such as hydrogen bonding, rather than covalent grafting(Paria & Khilar 2004). This adsorbed surfactant layer improved the wettability of the fibers and facilitated their separation in the aqueous medium. The adsorption mechanism can be expressed as follows:

$$\equiv Si\text{-}OH_{(surface)} + Tween\ 80_{(aq)} \rightleftharpoons \equiv Si\text{-}OH \cdots Tween\ 80_{(ads)}$$

The overall Tween 80-assisted dispersion process is illustrated in Fig**. 2**, including the untreated chopped fibers, treatment in aqueous solution, and the separated fibers after modification. The effectiveness of the treatment was further confirmed by the optical microscopy images shown in Fig**. 3**. As seen in Fig. **3**(**a**), the untreated chopped basalt fibers retained their bundled morphology with a fiber length of approximately 5 mm**,** whereas the modified fibers in Fig. **3**(**b**) exhibited a more separated and dispersed structure after Tween 80 treatment. This observation indicates that Tween 80 effectively reduced fiber agglomeration and promoted the dispersion of individual basalt fibers, which is beneficial for subsequent molding and uniform structure formation.

Fabrication of Basalt Fiber Foam

A circular frame of 29 mm diameter and 5 mm depth, along with its corresponding bottom plate, was fabricated using 3D printing and assembled prior to sample preparation. Basalt fibers were manually punched into the circular frame using tweezers to form an approximately 1 mm thick layer with nearly uniform distribution, as shown in Fig. **4**(**a**). For each layer, approximately 0.17 g of basalt fibers was used, and the

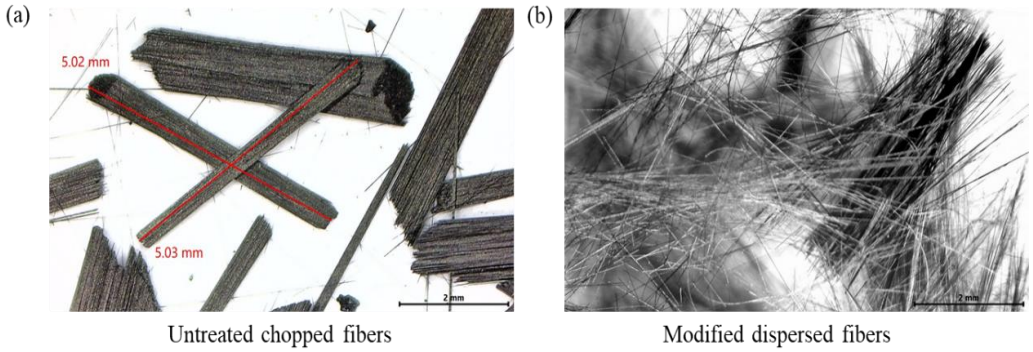

Figure 3: Optical microscopy images of basalt fibers: (a) untreated chopped fibers and (b) modified fibers after Tween 80-assisted dispersion treatment.

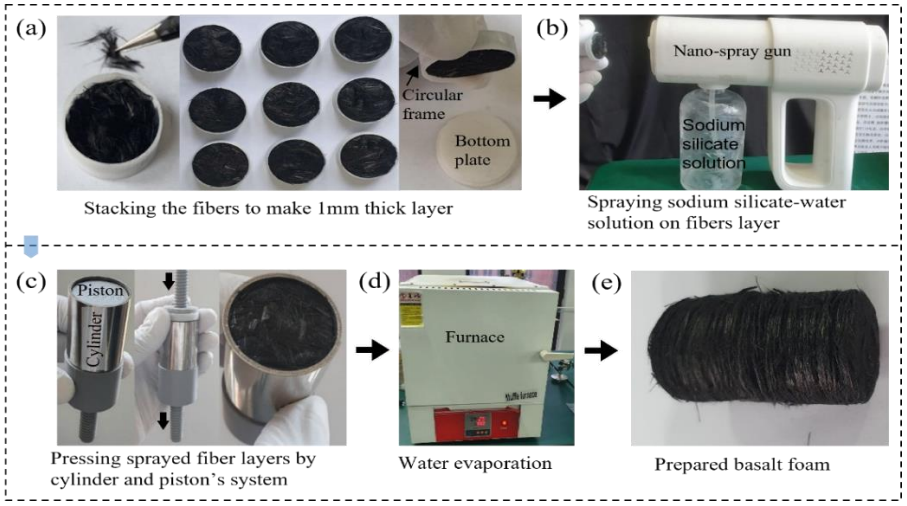

Figure 4: Schematic illustration of the basalt fiber foam fabrication process: (a) manual placement of basalt fibers in the 3D-printed circular frame, (b) spraying of sodium silicate binder solution, (c) compression using the piston-cylinder setup, (d) heat treatment in a muffle furnace, and (e) fabricated basalt fiber foam sample.

mass of the fibers was measured before compaction to improve reproducibility. The number of layers was selected according to the target sample thickness; for example,10, 20, 25, 30, and 50 layers were used to fabricate 10, 20, 25, 30, and 50 mm thick samples, respectively. A binder solution composed of 65% liquid sodium silicate and 35% distilled water was subsequently applied normal to the fiber layer using a nano-spray gun for approximately 1 s at a fixed distance of 10 cm. The same spraying time, spraying distance, and spraying direction were maintained for all layers and samples to control binder distribution. The spraying time was intentionally kept very short to avoid complete coating of the fiber surfaces and prevent pore blockage. Therefore, the binder was mainly deposited at selected fiber-fiber contact points to locally weld the fibers together, as illustrated in Fig. **4**(**b**). Based on the difference between the initial fiber mass and final sample mass, the retained binder content was estimated to be approximately 0.013-0.018 g per layer, corresponding to 7.27-9.57 wt.% of the final foam mass. This relatively low binder content indicates that the sodium silicate binder mainly served as a localized bonding phase at fiber-fiber contact points rather than filling the pore space or forming a continuous coating over the fibers. SEM observations also confirmed that the binder was mainly located at fiber-fiber contact points rather than forming a continuous coating over the fiber surfaces.

For compaction, a 3D-printed threaded piston system and a steel cylinder having the same diameter as the circular frame were used. After removal of the bottom plate, the sprayed basalt fiber layer was carefully placed on top of the steel cylinder and gently pressed using a second piston so that it was transferred onto the surface of the internal movable piston. Each layer was manually and gently pressed for approximately 2 s to obtain the desired layer thickness. The compaction process was mainly controlled by layer thickness rather than by applied force. After the first layer was compacted, the next fiber layer was prepared, sprayed, and placed with the sprayed side facing the already compacted layer. The layer was then gently compacted onto the previous layer. This spraying-stacking-compaction process was repeated layer by layer until the required final sample thickness was achieved, as shown in Fig. **4**(**c**). Thereafter, the 3D-printed piston assembly was removed, and the steel cylinder containing the compressed basalt fibers was placed in a muffle furnace at 150 °C for 3 h to evaporate water and promote effective bonding between fibers through the sodium silicate binder, as presented in Fig. **4**(**d**). After heating, the fabricated basalt fiber foam sample was removed from the cylinder, as shown in Fig. **4**(**c**). The final mass of each sample was also measured after fabrication, showing a slight increase due to binder addition. The reproducibility of the layer-by-layer fabrication method was supported by the small variation in bulk density among samples with different thicknesses.

Thermal Testing

The thermal response of the prepared BF was evaluated by direct flame exposure using the experimental setup shown in **Fig. 5**. In this test, a 30 mm thick BF sample was fixed on a metal mesh support attached to a vertical stand, while a micro torch was positioned in front of the sample to provide localized butane flame heating. The surface temperature evolution of the BF during flame exposure and the subsequent cooling stage was monitored using an infrared thermal camera (HIKMICRO H21ProS), which was fixed at a distance of 0.3 m from the sample. The thermal camera was set to capture images at 1 s intervals, and thermal images were recorded from the highest temperature state until the sample cooled down. The recorded thermal data were then used to analyze the surface temperature distribution of the BF through infrared thermal images, 3D surface temperature distributions, and temperature-time curves of selected monitoring points for quantitative evaluation of its thermal response.

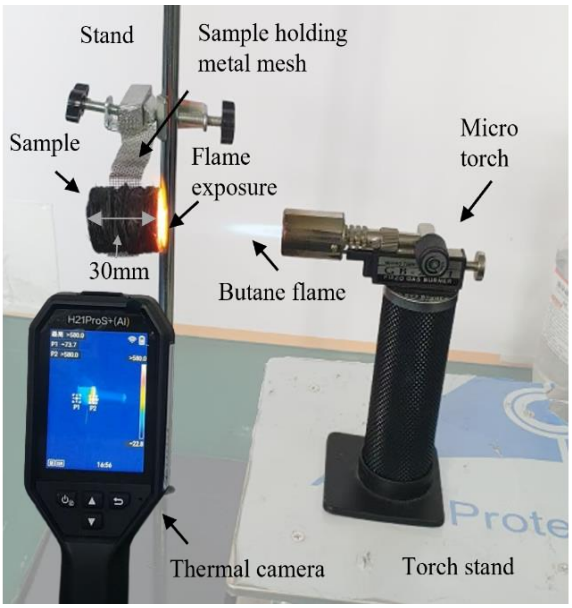

Figure 5: Experimental setup for thermal testing of basalt foam under direct butane flame exposure using an infrared thermal camera.

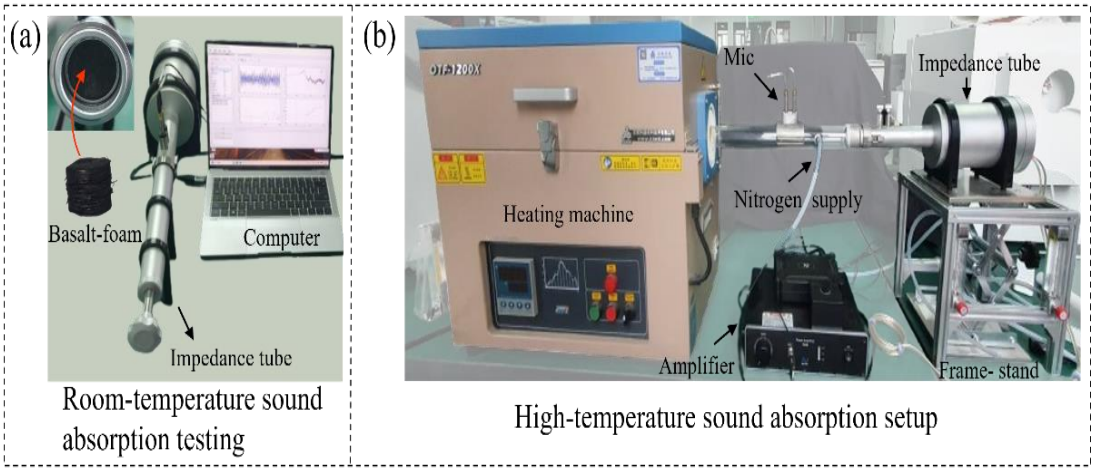

Figure 6: Sound absorption testing setup using the impedance tube system: (a) room-temperature measurement setup and (b) high-temperature measurement setup with nitrogen gas supply to prevent sample oxidation.

Sound Absorption Testing

The sound absorption performance of the prepared basalt fiber foam samples was evaluated using a 29 mm diameter impedance tube system (SW-4601) in accordance with ASTM E1050-12, over a frequency range of 450-6400 Hz. At room temperature, measurements were conducted for samples with thicknesses of 10, 20, 25, 30, and 50 mm, as shown in Fig. **6**(**a**). High-temperature measurements were further performed for the 50 mm thick sample at 200, 400, and 600 °C, using the setup shown in Fig. **6**(**b**). During the high-temperature tests, nitrogen gas was supplied to displace oxygen and minimize oxidation of the sample.

The normal-incidence sound absorption coefficient, α was determined using the transfer-function method and is given by

$$\alpha = 1 - |\mathrm{R}|^2 \tag{1}$$

where R is the normal-incidence sound pressure reflection coefficient at the sample surface, calculated as

$$\mathrm{R} = \frac{H_{12} - H_I}{H_R - H_{12}} e^{2jk_0x_1} \tag{2}$$

where H_{12} is the transfer function measured between the two microphones, x_1 is the distance from the first microphone to the sample surface, and k_0 is the wave number in air. The transfer functions of the incident and reflected waves are expressed as

$$H_I = e^{-jk_0s} \tag{3}$$

$$H_R = e^{jk_0s} \tag{4}$$

where s is the spacing between the two microphones(Chung & Blaser 1980a, 1980b).

To reduce experimental noise and clarify the frequency-dependent trend of the high-temperature sound absorption data, locally weighted scatterplot smoothing (LOWESS) was applied in MATLAB. In this method, a local weighted linear regression was fitted at each frequency point using neighboring data within a specified span. The regression coefficients were obtained by minimizing

$$\sum_{j \in N_i} \omega_{ij} \left[y_j - \left(\beta_0 + \beta_1 x_j \right) \right]^2 \tag{5}$$

where x_i and y_j denote the frequency and corresponding sound absorption coefficient, respectively, Ni represents the local neighborhood of the target point x_i, and ω_{ij} is the distance-based weight assigned to each neighboring data point(Cleveland 1979). A span value of 0.06 was used, indicating that 6% of the surrounding data points were included in each local regression. The smoothed sound absorption coefficient at each frequency was then obtained from the fitted local model, and the resulting values were constrained to the physical range of 0-1.

Compression Testing of Basalt Foam

The compressive behavior and structural integrity of the fabricated BF were evaluated using a universal testing machine. A 50 mm thick cylindrical BF specimen was placed between the compression plates and compressed under a uniaxial loading condition, as shown in Fig. **7**. The force-displacement response was recorded during compression to assess the load-bearing

behavior, deformation process, and structural stability of the foam. After unloading, the sample shape and height recovery were also examined to evaluate the ability of the basalt fiber network to maintain its structural integrity after large deformation. This test was used to determine whether the sodium-silicate-bonded BF could retain its porous framework during mechanical compression, which is important for handling, installation, and practical acoustic applications.

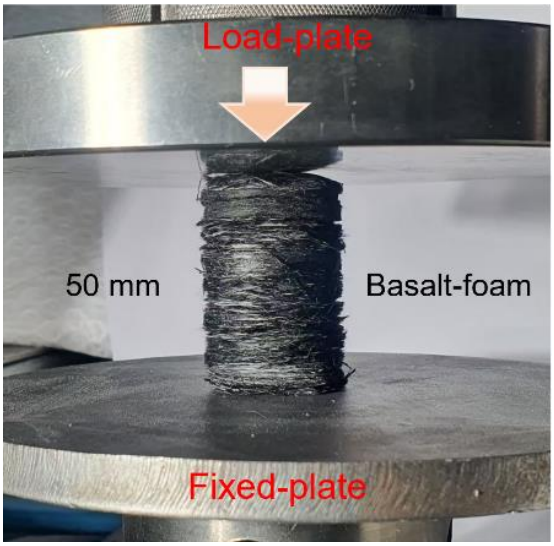

Figure 7: Compression testing setup for the 50 mm basalt foam specimen, showing the cylindrical foam placed between the upper load plate and lower fixed plate under uniaxial compression.

RESULTS AND DISCUSSION

Thermal Response of Basalt Foam

The corresponding infrared thermal images and 3D surface temperature distributions shown in **Fig. 8** indicate that the temperature rise was mainly concentrated in the flame-exposed region, while the remaining area of the sample exhibited a comparatively lower thermal response. Even after prolonged flame exposure, the temperature at monitoring point P1 did not increase excessively, suggesting that heat propagation through the BF remained limited and localized. After the flame was removed, the hot region gradually diminished, and the peak observed in the 3D thermal plots became lower and flatter with time, indicating progressive heat dissipation during cooling. A slight shift in the maximum-temperature position was also observed, which is likely associated with localized heat redistribution within the heterogeneous porous fiber network, where variations in fiber packing, inter-fiber contact, and local sodium silicate binder distribution can produce non-uniform heat conduction paths during cooling.

The temperature evolution curves of the monitoring points P1 and P2, presented in **Fig. 9**, further support this thermal behavior. In particular, the temperature at P2 dropped immediately within about 1 s after the flame was turned off, demonstrating a rapid response to the removal of the external heat source. The cooling process was characterized by an initially fast temperature decrease, followed by a slower decline as

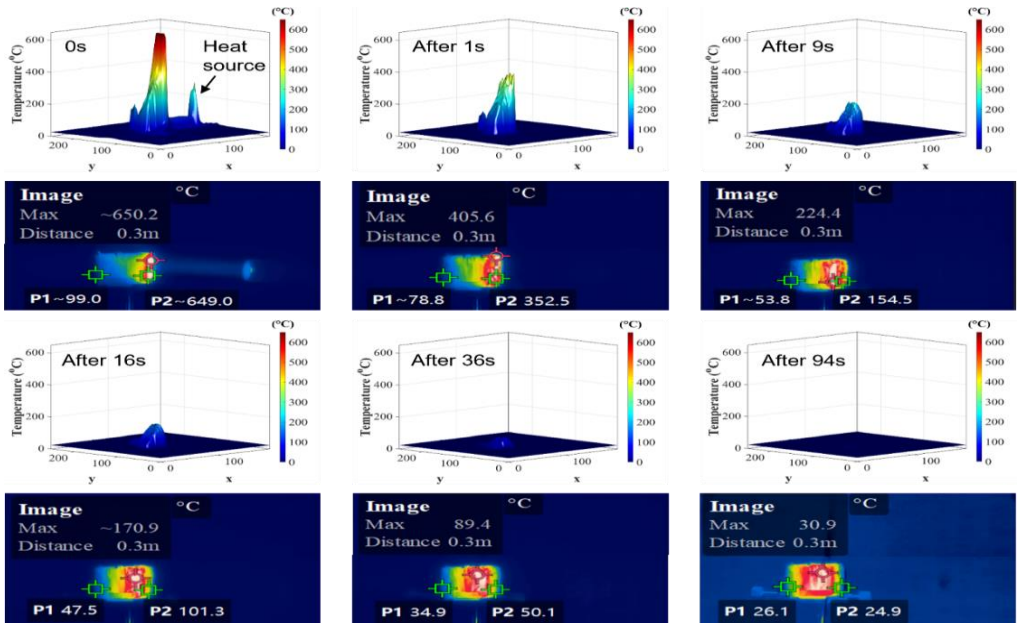

Figure 8: Infrared thermal images and corresponding 3D surface temperature distributions of basalt foam during cooling after flame exposure.

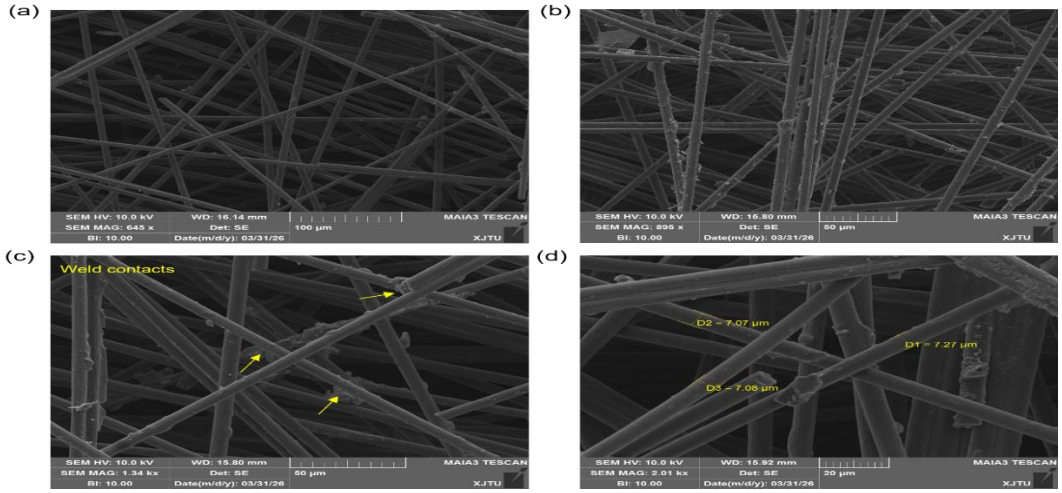

Figure 10: SEM images of basalt foam showing (a) randomly distributed fibrous porous structure, (b) localized sodium silicate binder deposits on fiber surfaces and junctions, (c) local binder-mediated bonding between adjacent fibers, and (d) basalt fiber diameter of approximately 7 µm.

the sample temperature gradually approached room temperature. From the highest recorded temperature to near room temperature, the total cooling time was approximately 94 s**,** indicating that the BF did not retain excessive heat for a prolonged period. This rapid cooling behavior, together with the confined high-temperature region observed in the thermal images, suggests that the porous BF can effectively restrict heat transfer while also dissipating stored heat relatively quickly. Importantly, despite direct flame exposure at high temperature, the sample maintained its structural integrity without obvious collapse or damage. These results demonstrate that the developed BF possesses promising thermal insulation and flame-resistant characteristics.

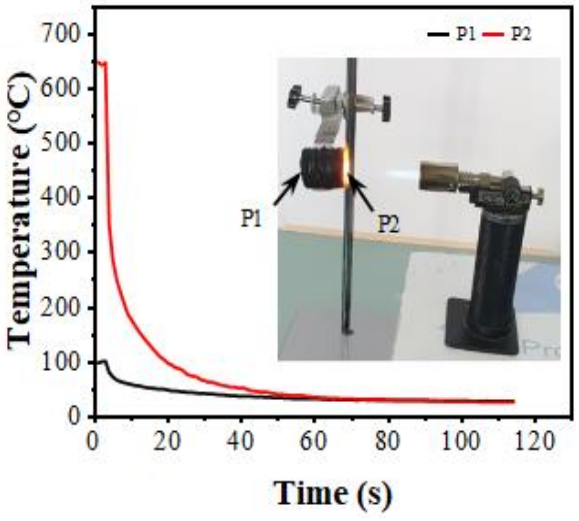

Figure 9: Temperature evolution curves of monitoring points P1 and P2 during cooling after flame exposure.

Microstructural and Physical Characterization of Basalt Foam

Microstructural morphology

As revealed by the SEM images**,** the fabricated BF possesses a three-dimensional fibrous structure composed of randomly distributed basalt fibers. As shown in **Fig. 10(a)**, the fibers are oriented in different directions and overlap with one another, producing abundant interconnected voids throughout the structure. This observation confirms that the foam retained a highly porous architecture after processing, which is important for maintaining open pore channels within the material. In **Fig. 10(b)**, the sodium silicate binder can be observed as localized deposits attached to the fiber surfaces and concentrated around several fiber junctions. This indicates that the binder was not uniformly coated over the entire fiber network, but instead remained mainly at specific regions of the structure. A clearer view is provided in **Fig. 10(c)**, where the binder is seen to locally connect adjacent fibers at their contact points, forming welded joints between neighboring fibers. Such localized bonding is beneficial because it helps preserve the structural integrity of the BF while avoiding complete blockage of the pore space. Furthermore, **Fig. 10(d)** shows that the individual basalt fibers possessed a relatively uniform diameter of approximately 7 µm, confirming the fine fibrous nature of the material. These SEM observations indicate that the fabricated BF consists of an interconnected porous fiber network with local binder-mediated bonding, which is favorable for maintaining both structural stability and open porosity.

Density and porosity

The bulk density and porosity of the basalt fiber foam were calculated to quantitatively describe the physical structure of the acoustic specimens. The bulk density of each cylindrical foam sample was determined from its measured mass and external volume. The external volume was calculated using:

$$V=\pi r^2 h \tag{6}$$

where *r* is the sample radius and *h* is the sample thickness. The bulk density was calculated as:

$$\rho_b=\frac{m}{V} \tag{7}$$

where *m* is the measured mass of the foam specimen and *V* is the external cylindrical volume. The measured masses of the 10, 20, 25, 30, and 50 mm thick samples were 1.8, 3.7, 4.6, 5.5, and 9.4 g, respectively. The skeletal density (ρ_s) of the basalt fiber framework was measured by helium pycnometry using a representative foam specimen. The measured skeletal density was 1.99643 g/cm³, with a relative standard deviation of 0.98%**,** indicating good repeatability of the true-density measurement. The porosity of each specimen was then calculated using:

$$\phi = \left(1-\frac{\rho_b}{\rho_s}\right)\times 100 \tag{8}$$

where ρ_b is the bulk density of the foam specimen obtained from helium pycnometry.

Table 1: The Bulk Density and Porosity of the Basalt Fiber Sample

Sample thickness (mm)	Mass (g)	External volume (cm^3)	Bulk density (g/cm^3)	Porosity (%)
10	1.8	6.61	0.273	86.35%
20	3.7	13.21	0.280	85.97%
25	4.6	16.51	0.279	86.05%
30	5.5	19.82	0.278	86.10%
50	9.4	33.03	0.285	85.74%
Average	-	-	0.279 ± 0.004	86.04 ± 0.23%

The calculated bulk density ranged from 0.273 to 0.285 g/cm³, with an average value of 0.279 ± 0.004 g/cm³. The corresponding porosity ranged from 85.74% to 86.35%, with an average value of 86.04 ± 0.23%. These results indicate that the fabricated BF has a highly porous structure with very consistent density among samples of different thicknesses. The low variation in bulk density also supports the reproducibility of the layer-by-layer fabrication method. The small and controlled binder addition also contributed to maintaining the high porosity of the foam which is favorable for acoustic absorption because it increases the available pore volume for sound wave penetration and enhances energy loss through internal friction within the fibrous network.

Airflow resistivity

Airflow resistivity was calculated from the impedance tube data using an image-based two-load method. In this method, the normalized surface impedance was obtained under two different boundary conditions: a rigid backing condition and a back-cavity condition. The measured normalized acoustic resistance and reactance were used to calculate the normalized characteristic impedance and complex wave number of the porous foam. The airflow resistivity was then obtained using:

$$\sigma(f) = -\rho_0 c_0 \mathrm{Im}(z_m k_m) \tag{9}$$

where ρ_0 is the air density, c_0 is the speed of sound in air, z_m is the normalized characteristic impedance of the porous material, and k_m is the complex wave number. In the calculation, ρ_0=1.204 kg/m³ and c_0=343 m/s were used. The final airflow resistivity averaged over the stable frequency range was σ =5.9206×104 Pa s/m² with a standard deviation of *SD*=5.9669×102 Pa s/m² and a coefficient of variation of *CV*= (*SD*/σ)×100=1.01%.

The low coefficient of variation indicates that the calculated airflow resistivity remained stable within the selected frequency range, supporting the reliability of the averaged value. From an acoustic point of view, airflow resistivity is a key parameter because it controls the resistance experienced by oscillating air particles inside the porous structure. If the airflow resistivity is too low, sound waves can pass through the material with limited dissipation. If it is too high, sound waves are mainly reflected from the surface. Therefore, the measured airflow resistivity of approximately 5.92 × 10⁴ Pa·s/m²**,** together with the high porosity and low bulk density, suggests that the BF provides a suitable porous structure for acoustic wave penetration and internal viscous dissipation.

Room-Temperature Sound Absorption of Basalt fiber

As shown in Fig. **11**, the room-temperature sound absorption of BF was strongly dependent on sample thickness and frequency. The absorption curves are presented as the mean values with standard deviation (±SD), obtained from repeated acoustic measurements, to demonstrate the repeatability and reliability of the impedance tube results. All samples showed relatively lower absorption at low frequencies, followed by increased absorption with increasing frequency, which is typical for porous fibrous absorbers.

The frequency-dependent absorption behavior is closely related to the open pore structure, tortuous sound propagation pathways, and randomly entangled basalt fiber network. At low frequencies, the acoustic wavelength is relatively large compared with the pore size and sample thickness; therefore, sound waves interact less effectively with the internal pore walls, resulting in lower acoustic energy dissipation. As frequency increases, the oscillating air particles experience stronger interaction with the pore walls and fiber surfaces. The tortuous pathways created by the interconnected fiber network increase the effective propagation distance inside the foam, thereby enhancing viscous friction and thermal exchange at the fiber-air interfaces.

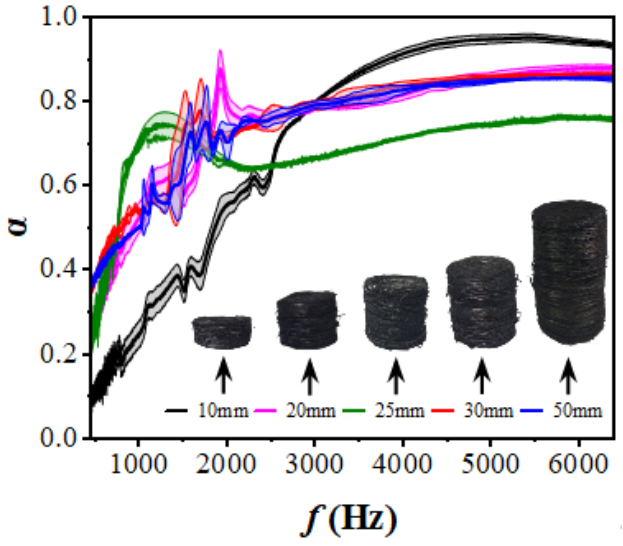

Figure 11: Room-temperature normal-incidence sound absorption coefficient of basalt foam samples with different thicknesses. The curves represent the mean absorption coefficient obtained from repeated measurements, and the shaded regions indicate the standard deviation (±SD). Insets show the corresponding basalt foam samples with thicknesses of 10, 20, 25, 30, and 50 mm.

The 10 mm sample showed a sharp rise and reached the highest peak absorption coefficient of approximately 0.960 near 4734 Hz, but its curve fluctuated noticeably in the low-to-mid frequency region, indicating a less stable absorption response. This behavior may be attributed to the limited thickness and shorter acoustic path length, which can produce localized resonance-like absorption rather than stable broadband dissipation. The 20 mm sample reached a peak value of about 0.922 near 1724 Hz and then maintained relatively high absorption at higher frequencies. The 25 mm sample showed a rapid early increase, reaching approximately 0.74-0.75 around 1000-1200 Hz, followed by a slight reduction in the mid-frequency region and a gradual recovery toward higher frequencies. This indicates that the 25 mm sample provided effective low-to-mid frequency absorption, although its high-frequency absorption remained lower than that of the thicker 30 and 50 mm samples.

The 30 and 50 mm samples exhibited smoother and more broadband absorption behavior. The 30 mm sample gradually increased with frequency and reached a peak absorption coefficient of approximately 0.865 near 5518 Hz, while the 50 mm sample reached about 0.854 near 5366 Hz and maintained stable absorption over a wide high-frequency range. The improved broadband response of the thicker samples can be attributed to the longer acoustic propagation path inside the foam, which increases repeated interaction between oscillating air particles and the tortuous basalt fiber network. In thicker samples, sound waves travel through a larger volume of interconnected pores, increasing the probability of multiple scattering, frictional loss, and thermal dissipation. The randomly distributed basalt fibers also act as internal obstacles that disturb air-particle motion and improve acoustic damping. Therefore, the thinner samples produced higher localized peaks, whereas the thicker samples showed more stable broadband absorption. The 25 mm sample offered an intermediate response with earlier absorption in the low-to-mid frequency range, while the 30 and 50 mm samples benefited from greater thickness, higher tortuous path length, and more effective fiber-network dissipation over a broader frequency range.

High-Temperature Sound Absorption of Basalt fiber

As shown in Fig. **12**, the 50 mm BF maintained strong sound absorption performance under elevated-temperature conditions. At all tested temperatures, the absorption coefficient increased with frequency, confirming that the material remained particularly

effective in the medium- and high-frequency regions. The sample tested at 200 °C showed the best overall performance, reaching a peak absorption coefficient of approximately 0.956, followed by the 400 °C and 600 °C conditions with peak values of about 0.948 and 0.932, respectively. Although a slight reduction in absorption was observed at higher temperatures, especially at 600 °C, the overall acoustic response remained high.

The temperature-dependent absorption behavior can be explained by changes in the thermophysical properties of the pore air. As temperature increases, the dynamic viscosity of air increases, which strengthens viscous interaction between oscillating air particles and the internal fiber surfaces. This can enhance acoustic energy dissipation inside the pore network, especially when the foam maintains open and interconnected pores. However, elevated temperature also changes air density, sound speed, wavelength, and acoustic impedance, which can shift the impedance matching condition between the incident sound wave and the porous foam. Therefore, the improvement at 200 °C and 400 °C suggests that the BF achieved favorable viscous dissipation and impedance matching within the tested frequency range. At 600 °C, the slight decrease in absorption may be related to stronger mismatch between the heated pore-air medium and the surrounding acoustic field, reducing part of the incident wave penetration into the porous structure. Nevertheless, the high absorption retained at 600 °C confirms that the BF preserved its acoustic functionality and structural stability under severe thermal conditions.

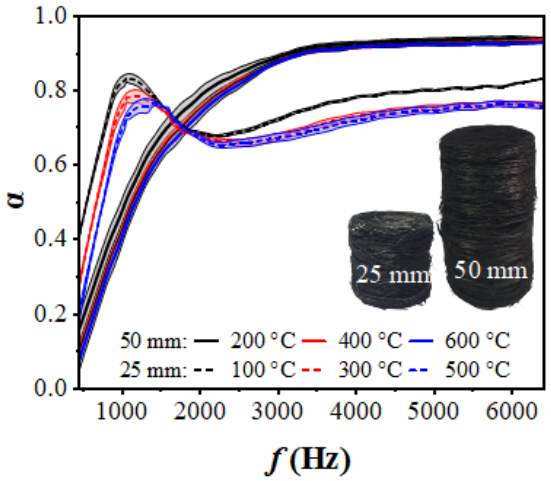

Figure 12: High-temperature normal-incidence sound absorption coefficient of 25 and 50 mm basalt foam samples. The curves represent mean absorption coefficient values, and the shaded regions indicate the standard deviation (±SD). Insets show the corresponding 25 and 50 mm basalt foam samples.

The elevated-temperature acoustic measurements were conducted under a nitrogen atmosphere to minimize oxidative effects during testing. Under practical service conditions, however, the foam may be exposed to air or other oxidative environments for extended periods. In this study, direct thermal/fire exposure testing at 650 °C and high-temperature acoustic testing at 600 °C showed that the BF and sodium silicate binder maintained good short-term thermal stability. These results indicate that the inorganic basalt fiber network and binder phase can withstand severe thermal conditions without immediate structural failure. However, long-term exposure in oxidative atmospheres may still influence the fiber-binder contact points through thermal aging, local embrittlement, microcrack formation, or gradual weakening of inter-fiber bonding. Such changes could alter the pore structure, airflow resistivity, and acoustic dissipation behavior over time. Therefore, long-term thermal aging in air, followed by post-aging acoustic and mechanical testing, should be considered in future work to further evaluate service durability under oxidative conditions.

ACOUSTIC RESPONSE OF BASALT FOAM AT ELEVATED TEMPERATURES

The acoustic response of BF at room and elevated temperatures is compared in Fig. **13**. For the 50 mm sample, shown in Fig. **13**(**a**), the absorption coefficient increased progressively with frequency under all temperature conditions. A clear high-absorption region was observed between approximately 1800 and 6400 Hz, where the absorption coefficient remained mainly within 0.70-0.95. The elevated-temperature curves, especially at 200 and 400 °C, entered this high-performance region earlier and maintained higher absorption than the room-temperature curve over most of the medium- and high-frequency range. This behavior indicates that heating enhanced acoustic dissipation inside the pore network, most likely due to increased pore-air viscosity and stronger frictional interaction between oscillating air particles and the basalt fiber surfaces. At 600 °C, the absorption slightly decreased compared with 200 and 400 °C, but it still remained within the high-absorption zone over a broad frequency range, confirming that the 50 mm BF retained effective acoustic damping under severe thermal conditions.

The 25 mm sample, shown in Fig. **13**(**b**), exhibited a different but still stable temperature-dependent response. The shaded region indicates absorption coefficients of approximately 0.64-0.84 over the frequency range of about 694-6400 Hz. Unlike the 50

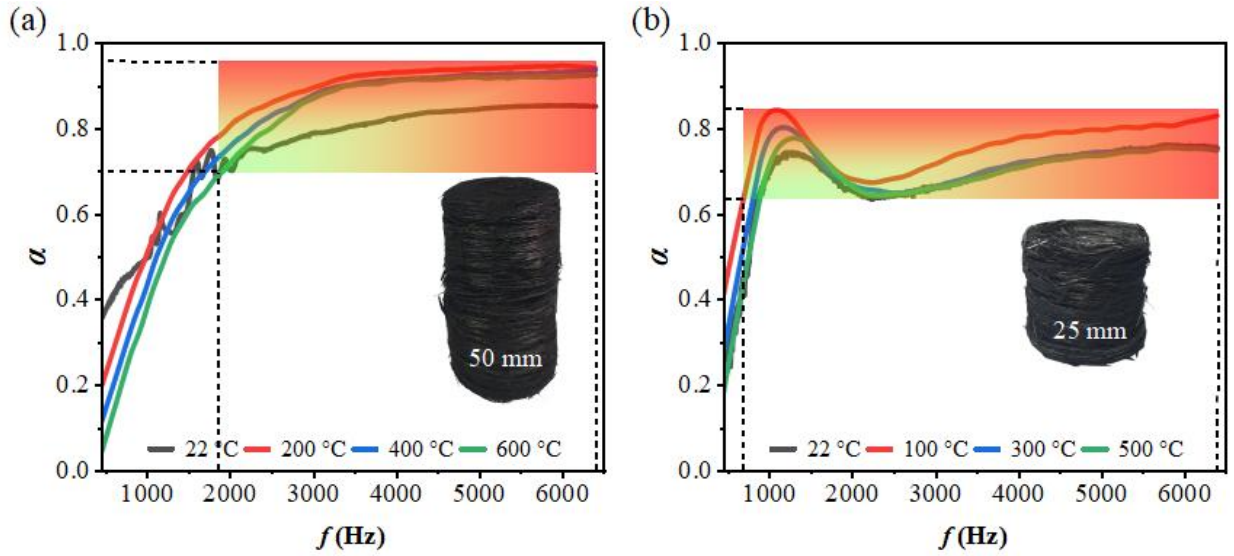

Figure 13: Temperature-dependent sound absorption response of basalt foam: (a) 50 mm sample tested at 22, 200, 400, and 600 °C, and (b) 25 mm sample tested at 22, 100, 300, and 500 °C. The shaded regions indicate the effective high-absorption frequency ranges.

mm sample, the 25 mm foam showed an early absorption peak near 1000-1200 Hz, followed by a moderate decrease around 1800-2500 Hz and then a gradual recovery toward higher frequencies. This behavior suggests that the thinner sample was more sensitive to impedance matching and resonance-related effects at lower frequencies. The room-temperature and 100 °C curves showed stronger absorption at higher frequencies, whereas the 300 and 500 °C curves remained slightly lower after the initial peak. This reduction at higher temperatures may be related to changes in pore-air density, sound speed, and acoustic impedance, which can reduce sound penetration despite increased viscous losses. Nevertheless, the 25 mm BF maintained absorption mostly above 0.64 across a wide frequency range, demonstrating that even the thinner configuration preserved effective acoustic performance at elevated temperatures.

The comparison between Fig. **13**(**a**) and Fig. **13**(**b**) shows that thickness strongly affected the high-temperature acoustic response. The 50 mm sample provided broader and more sustained absorption at medium and high frequencies, while the 25 mm sample produced an earlier absorption peak and maintained moderate-to-high absorption over a wide range. These results indicate that the BF's acoustic performance is governed by the combined effects of sample thickness, pore-air thermophysical changes, and internal viscous/thermal dissipation within the interconnected fibrous network.

COMPARATIVE EVALUATION WITH COMMERCIAL AND LITERATURE-REPORTED HIGH-TEMPERATURE ACOUSTIC ABSORBERS

To evaluate the practical acoustic performance of the developed BF, the 25 mm thick BF was compared with commercial and literature-reported high-temperature sound-absorbing materials, as shown in Fig. **14**(**a**-**c**). Since available studies on high-temperature sound absorption are still limited, especially for materials tested under comparable thickness and temperature conditions, the comparison was made using the most relevant commercial data sheet and literature-reported fibrous/porous metal absorbers. Because the reported frequency ranges are different among the reference materials, each comparison was discussed within the frequency range available from the corresponding reference data.

In Fig. **14**(**a**), the room-temperature absorption performance of the BF is compared with the commercial 3M™ Thinsulate™ High Temperature Acoustic Absorber HT500P/HT500PP (3M Company 2021). According to the 3M technical data sheet, HT500P/HT500PP has a nominal thickness of 26 mm and its normal-incidence absorption coefficient is reported according to ASTM E-1050, making it a suitable commercial benchmark for comparison with the 25 mm BF. The 3M absorber shows strong broadband absorption, particularly at lower and mid-frequency regions, where its absorption coefficient rapidly increases and remains high over a wide frequency range. In comparison, the BF shows lower

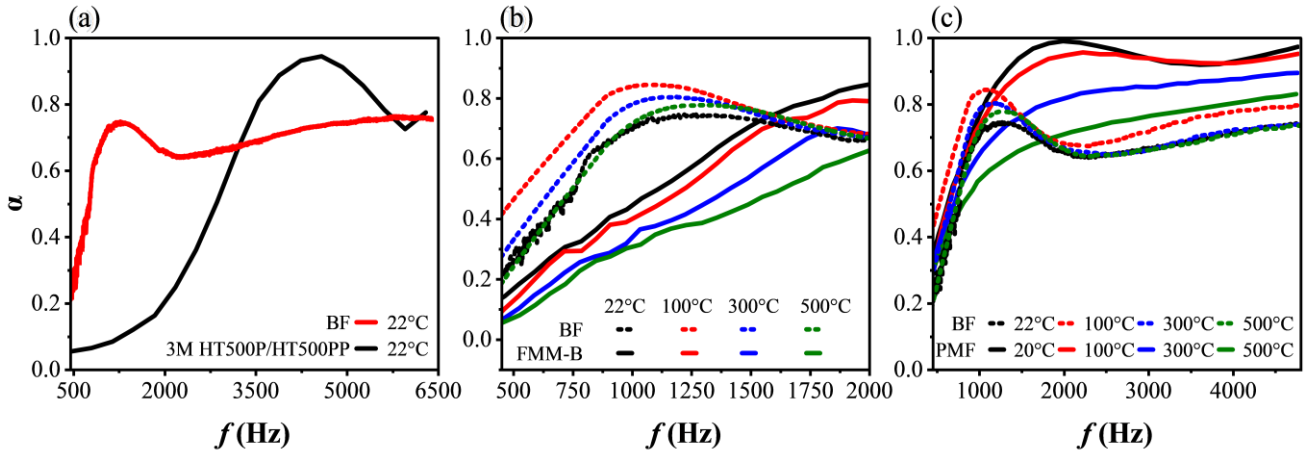

Figure 14: Comparative sound absorption performance of the developed basalt foam () with commercial and literature-reported absorbers: **(a)** vs 3M™ Thinsulate™ High Temperature Acoustic Absorber HT500P/HT500PP, **(b)** vs fibrous metal material Sample B (FMM-B) reported by Sun *et al.*, and **(c)** vs porous metal fiber (PMF) reported in the literature. The comparisons are presented over the available frequency ranges of the corresponding reference materials.

absorption at low frequencies but its absorption coefficient increases significantly at higher frequencies, reaching values above 0.8 in the high-frequency region. This indicates that although the commercial 3M absorber provides better broadband acoustic performance at room temperature, the BF still exhibits competitive high-frequency absorption while offering the additional advantage of inorganic thermal stability. It should also be noted that the 3M data sheet reports typical normal-incidence acoustic absorption according to ASTM E-1050, while its high-temperature information mainly refers to thermal durability, specifically no disintegration up to 150 °C for 336 h or 180 °C for 48 h, rather than acoustic absorption measured at elevated temperature.

Fig. **14**(**b**) compares the BF with fibrous metal material Sample B reported by Sun et al in the literature(Sun *et al.* 2010). The comparison is particularly relevant because Sample B has the same thickness of 25 mm and a similar porosity level of approximately 85%, close to the porosity of the present BF. The comparison was made over the 500-2000 Hz range reported for the fibrous metal material. The BF exhibits higher absorption than the fibrous metal material in the low-to-mid frequency region, especially below approximately 1500 Hz. The BF reaches its main absorption peak around 900-1200 Hz, whereas the fibrous metal material shows a gradual increase in absorption with frequency. At higher frequencies near 1800-2000 Hz, the fibrous metal material approaches or exceeds some BF curves, indicating stronger high-frequency improvement in that range. With increasing temperature from room temperature to 500 °C, the BF shows a reduction in absorption coefficient, which is consistent with the high-temperature trend reported for fibrous materials, where changes in air viscosity, acoustic resistance, and acoustic reactance influence sound wave dissipation.

Fig. **14**(**c**) further compares the BF with the porous metal fiber material reported in the previous study(Zhang *et al.* 2018). Both materials have comparable thickness, and the comparison shows that the BF performs well in the lower frequency region, especially around its absorption peak near 900-1100 Hz. However, the porous metal fiber material shows stronger broadband absorption at higher frequencies, particularly above approximately 1500 Hz, where its absorption coefficient remains higher and more stable. This difference may be related to differences in pore structure, fiber arrangement, tortuosity, and flow resistance between the two materials. The BF shows a more pronounced peak-dip behavior, suggesting that its absorption is more frequency-dependent, while the porous metal fiber material provides broader high-frequency absorption. Nevertheless, the BF maintains useful sound absorption even at 600 °C, confirming that the developed inorganic fibrous foam is suitable for elevated-temperature acoustic applications.

Overall, Fig. **14** demonstrates that the developed BF has a clear practical advantage as a lightweight inorganic absorber capable of maintaining sound absorption at elevated temperatures up to 500 °C. Compared with the commercial 3M absorber, the BF is less effective at room-temperature broadband absorption but can be tested and used at much higher

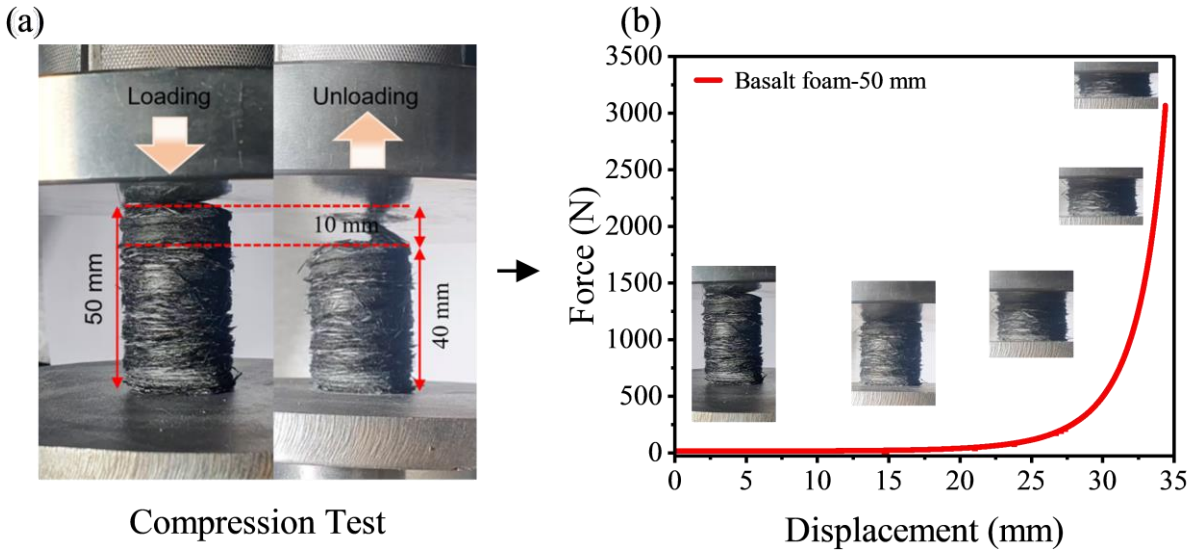

Figure 15: Compression behavior and structural integrity of the 50 mm basalt foam: (a) photographs of the sample during loading and after unloading, showing recovery to approximately 40 mm after compression and a permanent height loss of about 10 mm; (b) force-displacement curve of the 50 mm basalt foam with inset images showing progressive deformation during compression.

temperatures. Compared with fibrous and porous metal materials, the BF shows competitive low-to-mid frequency absorption, although further optimization of pore structure, tortuosity, and airflow resistivity may be needed to improve its broadband high-frequency performance.

Compressive Behavior and Structural Stability of Basalt Foam

The compressive behavior of the 50 mm BF was evaluated to assess its mechanical integrity and structural stability, as shown in Fig. **15**. According to the force-displacement data, the sample was compressed up to a maximum displacement of approximately 34.57 mm, corresponding to a compressed height of about 15.43 mm from the original 50 mm height as shown in Fig. **15**(**a**). The maximum force reached approximately 3062 N near the final compression stage. The maximum compressive stress was estimated using:

$$\sigma_c = \frac{F_{max}}{A} \quad (10)$$

where σ_c is the compressive stress, F_{max} is the maximum compressive force, and A is the cross-sectional area of the sample. Based on the sample diameter of 29 mm, the cross-sectional area was approximately 660.5 mm². Therefore, using F_{max} = 3062 N, the estimated maximum compressive stress was approximately 4.64 MPa. After unloading, the sample recovered to approximately 40 mm, indicating about 80% height recovery, while the remaining 10 mm height loss represents permanent deformation.

The force-displacement curve in Fig. **15**(**b**) shows a typical compression response of a highly porous fibrous material. In the initial region, the force increased slowly with displacement, indicating that deformation was mainly governed by bending, sliding, and rearrangement of the loosely connected basalt fibers. As compression continued, the pore structure progressively collapsed and the fiber network became more compact. At larger displacement, the force increased sharply, corresponding to the densification stage, where collapsed fibers came into close contact and strongly resisted further deformation.

The partial recovery after unloading indicates that the BF contains both recoverable and irreversible deformation components. The recoverable deformation is associated with elastic spring-back of the interconnected basalt fiber network, whereas the permanent deformation is mainly attributed to local pore collapse, fiber rearrangement, and partial debonding at fiber-fiber contact points. Importantly, the sample retained its overall cylindrical shape after unloading and did not disintegrate, confirming that the sodium-silicate-bonded basalt fiber framework provided sufficient structural integrity. This structural stability is important for practical acoustic applications because the foam must maintain its porous skeleton during handling, installation, and elevated-temperature operation.

CONCLUSION

A porous BF was successfully fabricated using Tween 80-assisted fiber dispersion, sodium silicate-mediated local bonding, and layer-wise compaction. The foam exhibited an open and interconnected fibrous structure, with the binder mainly located at fiber-fiber contact points. The measured bulk density and porosity were approximately 0.280 ± 0.003 g/cm^3 and 85.96 ± 0.16%, respectively, while the airflow resistivity was 5.9206 × 10^4 Pa·s/m², confirming a highly porous structure suitable for acoustic energy dissipation. The thermal and acoustic results showed that the BF retained its structural and functional stability under severe conditions. Direct flame exposure produced localized heating followed by rapid cooling, without obvious structural collapse. The 50 mm foam maintained strong sound absorption at 200, 400, and 600 °C, indicating that the basalt fiber network and sodium silicate binder remained effective at elevated temperature. Room-temperature results further showed that sound absorption depended strongly on thickness and frequency, with thicker samples providing broader and more stable absorption due to longer acoustic pathways, higher tortuosity, and enhanced viscous/thermal dissipation. The comparison with commercial and literature-reported absorbers showed that the BF provides competitive low-to-mid frequency absorption and useful high-temperature acoustic stability, although its low-frequency absorption remains limited. Compression testing also confirmed adequate structural integrity, with a maximum force of approximately 3062 N, an estimated compressive stress of 4.64 MPa, and about 80% height recovery after unloading.

Overall, the developed BF is a promising inorganic absorber for high-temperature noise-control applications. Future work should focus on improving low-frequency absorption through gradient pore structures, multilayer designs, optimized airflow resistivity and tortuosity, or the use of an air-back cavity/perforated facing layer. Long-term oxidative thermal aging, followed by acoustic and mechanical testing, should also be conducted to evaluate service durability under practical conditions.

DECLARATION OF COMPETING INTEREST

The authors declare that they have no known competing financial interests or personal relationships that could have appeared to influence the work reported in this paper.

DATA AVAILABILITY

Data will be made available on request.

FUNDING STATEMENT

The funding source for this study provided by the “Young Talent Support Plan” of Xi’an Jiaotong University: JCYJ20210324115412035 and funding number is: LX6J021.

REFERENCES

References

3M Company. 3M™ Thinsulate™ High Temperature Acoustic Absorber HT Series. Technical Data Sheet. 2021. https://multimedia.3m.com/mws/media/1224434O/3m-tm-thinsulate-high-temperature-acoustic-absorber.pdf

Bai, P., Yang, X., Shen, X., Zhang, X., Li, Z., Yin, Q., Jiang, G. & Yang, F. Sound absorption performance of the acoustic absorber fabricated by compression and microperforation of the porous metal. Materials & Design, 2019. 167: p. 107637. https://doi.org/10.1016/j.matdes.2019.107637

Buratti, C., Moretti, E., Belloni, E. & Agosti, F. Thermal and acoustic performance evaluation of new basalt fiber insulation panels for buildings. Energy Procedia, 2015. 78: p. 303–308. https://doi.org/10.1016/j.egypro.2015.11.648

Cao, L., Fu, Q., Si, Y., Ding, B. & Yu, J. Porous materials for sound absorption. Composites Communications, 2018. 10: p. 25–35. https://doi.org/10.1016/j.coco.2018.05.001

Cao, L., Shan, H., Zong, D., Yu, X., Yin, X., Si, Y., Yu, J. & Ding, B. Fire-resistant and hierarchically structured elastic ceramic nanofibrous aerogels for efficient low-frequency noise reduction. Nano Letters, 2022. 22(4): p. 1609–1617. https://doi.org/10.1021/acs.nanolett.1c04532

Chen, Y., Wu, F., Yu, Q. & Brouwers, H.J.H. Bio-based ultra-lightweight concrete applying miscanthus fibers: Acoustic absorption and thermal insulation. Cement and Concrete Composites, 2020. 114: p. 103829. https://doi.org/10.1016/j.cemconcomp.2020.103829

Cheng, B., Gao, N., Huang, Y. & Hou, H. Broadening perfect sound absorption by composite absorber filled with porous material at low frequency. Journal of Vibration and Control, 2022. 28(3–4): p. 410–424. https://doi.org/10.1177/1077546320980214

Chung, J.Y. & Blaser, D.A. Transfer function method of measuring in-duct acoustic properties. I. Theory. The Journal of the Acoustical Society of America, 1980a. 68(3): p. 907–913. https://doi.org/10.1121/1.384778

Chung, J.Y. & Blaser, D.A. Transfer function method of measuring in-duct acoustic properties. II. Experiment. The Journal of the Acoustical Society of America, 1980b. 68(3): p. 914–921. https://doi.org/10.1121/1.384779

Cleveland, W.S. Robust Locally Weighted Regression and Smoothing Scatterplots. Journal of the American Statistical Association, 1979. 74(368): p. 829–836. https://doi.org/10.1080/01621459.1979.10481038

Feng, Z. & Liu, Y. The latest research status of porous sound-absorbing materials. Journal of Polymer Engineering, 2025. 45(3): p. 207–225. https://doi.org/10.1515/polyeng-2024-0211

Fiore, V., Scalici, T., Di Bella, G. & Valenza, A. A review on basalt fibre and its composites. Composites Part B: Engineering, 2015. 74: p. 74–94.

https://doi.org/10.1016/j.compositesb.2014.12.034

Jamshaid, H. & Mishra, R. A green material from rock: basalt fiber – a review. The Journal of The Textile Institute, 2016. 107(7): p. 923–937. https://doi.org/10.1080/00405000.2015.1071940

Kang, S. & Jeong, H.Y. Sorption of a nonionic surfactant Tween 80 by minerals and soils. Journal of Hazardous Materials, 2015. 284: p. 143–150. https://doi.org/10.1016/j.jhazmat.2014.11.010

Li, X., Xu, T., Wu, W., Yang, J. & Cai, X. High-temperature sound absorption characteristics of microlattice materials backed with a resonant cavity. Journal of Vibration and Acoustics, 2026. 148(1): p. 010503. https://doi.org/10.1115/1.4070063

Li, Z., Wang, Z., Guo, Z., Wang, X. & Liang, X. Ultra-broadband sound absorption of a hierarchical acoustic metamaterial at high temperatures. Applied Physics Letters, 2021. 118(16): p. 161903. https://doi.org/10.1063/5.0044656

Lomte, A., Xue, Y., Johnston, W., Song, G., Bolton, J.S. & Sharma, B. Acoustic modeling of three-dimensional-printed fibrous sound absorbers. The Journal of the Acoustical Society of America, 2024. 156(6): p. 3757–3771. https://doi.org/10.1121/10.0034429

Lou, J., He, C., Shui, A. & Yu, H. Enhanced sound absorption performance of porous ceramics with closed-pore structure. Ceramics International, 2023. 49(23): p. 38103–38114. https://doi.org/10.1016/j.ceramint.2023.09.140

Ma, X. & Su, Z. Development of acoustic liner in aero engine: a review. Science China Technological Sciences, 2020. 63(12): p. 2491–2504. https://doi.org/10.1007/s11431-019-1501-3

Moretti, E., Belloni, E. & Agosti, F. Innovative mineral fiber insulation panels for buildings: Thermal and acoustic characterization. Applied Energy, 2016. 169: p. 421–432. https://doi.org/10.1016/j.apenergy.2016.02.048

Paria, S. & Khilar, K.C. A review on experimental studies of surfactant adsorption at the hydrophilic solid–water interface. Advances in Colloid and Interface Science, 2004. 110(3): p. 75–95. https://doi.org/10.1016/j.cis.2004.03.001

Paun, F., Gasser, S. & Leylekian, L. Design of materials for noise reduction in aircraft engines. Aerospace Science and Technology, 2003. 7(1): p. 63–72. https://doi.org/10.1016/S1270-9638(02)00006-8

Song, S., Lyu, Y., Zhao, J., Ren, W., Wang, J., Li, L., Wang, Q. & Zhang, M. Broadband sound absorption cellulose/basalt fiber composite paper with excellent thermal insulation and hydrophobic properties. Industrial Crops and Products, 2024. 218: p. 118985. https://doi.org/10.1016/j.indcrop.2024.118985

Spillere, A.M., Braga, D.S., Seki, L.A., Bonomo, L.A., Cordioli, J.A., Rocamora, B.M., Greco, P.C., Dos Reis, D.C. & Coelho, E.L. Design of a single degree of freedom acoustic liner for a fan noise test rig. International Journal of Aeroacoustics, 2021. 20(5–7): p. 708–736. https://doi.org/10.1177/1475472X211023831

Sun, F., Chen, H., Wu, J. & Feng, K. Sound absorbing characteristics of fibrous metal materials at high temperatures. Applied Acoustics, 2010. 71(3): p. 221–235. https://doi.org/10.1016/j.apacoust.2009.09.001

Tang, X. & Yan, X. Acoustic energy absorption properties of fibrous materials: a review. Composites Part A: Applied Science and Manufacturing, 2017. 101: p. 360–380. https://doi.org/10.1016/j.compositesa.2017.07.002

Wang, H., Chen, Q., Chen, M., Zhang, J.Z. & Liu, Y.S. Novel filter material by glass fiber foam laying for nonwoven fabrics. Journal of Industrial Textiles, 2023. 53: p. 1–13. https://doi.org/10.1177/15280837231199259

Yang, M., Ding, Y., Chen, Z., Wu, Q., Liu, L., Liu, T., Li, M., Xu, K., Le, L. & Yang, L. Layered ZrO_2/SiO_2 aerogel composite fibrous flexibility membrane for thermal insulation and sound absorption. Journal of the American Ceramic Society, 2024. 107(6): p. 4307–4320. https://doi.org/10.1111/jace.19704

Zhang, J., Chen, W., Ren, S., Xin, F., Chen, T. & Lu, T.J. Sound absorbing properties and optimization design of gradient porous metal fibers in high-temperature environments. Journal of Xi'an Jiaotong University, 2018. 52(1): p. 143. https://doi.org/10.7652/xjtuxb201801021

Zhang, P., Zhao, S., Li, K., Zhang, Z., Yang, F., Li, X., Song, Y., Gan, Z. & Yang, Z. Large-scale production of elastic SiC/SiO_2 nanofibrous composite aerogels with a labyrinth structure for high-temperature insulation, fire prevention, and noise absorption. Chemical Engineering Journal, 2025. 505: p. 159166. https://doi.org/10.1016/j.cej.2024.159166

Zhang, Q., Huang, H., Lei, C., Liu, Y. & Li, W. Review of lightweight, high-temperature thermal insulation materials for aerospace. Materials, 2025. 18(10): p. 2383. https://doi.org/10.3390/ma18102383

Zong, D., Bai, W., Geng, M., Yin, X., Yu, J., Zhang, S. & Ding, B. Bubble templated flexible ceramic nanofiber aerogels with cascaded resonant cavities for high-temperature noise absorption. ACS Nano, 2022. 16(9): p. 13740–13749. https://doi.org/10.1021/acsnano.2c06011

Received on 11-05-2026 Accepted on 03-06-2026 Published on 09-06-2026

https://doi.org/10.65904/3083-3604.2026.02.06